THE ASTROPHYSICAL JOURNAL, 430:743–756, 1994 August 1

MAGNETIC FIELD STRUCTURE IN MONOCEROS R2

T. H. JARRETT,[1,2] G. NOVAK,[2,3] T. XIE,[2,4,5] AND P. F. GOLDSMITH[2,4,6]

Received 1993 September 7; accepted 1994 January 27

ABSTRACT

We have carried out polarimetric observations to investigate the geometry of the magnetic field in the giant molecular cloud Monoceros R2. This study is based upon deep *R*-band CCD polarimetry, covering a total area of 0.5 deg^2 of the giant molecular cloud. The data were calibrated using a new technique that relies on obtaining broad-band photometry of stars simultaneously with polarimetric photometry of the Mon R2 fields, thus providing an accurate means of measuring the electric vectors of starlight which is polarized by the foreground dust grains aligned by the magnetic field in the Mon R2 GMC. In this work, (1) we were able to continuously trace magnetic field lines from the largest scales in Mon R2 to the detailed structure of the field in the dense core, as determined from infrared polarimetry; and (2) we have found that the ambient field is apparently modified by a large-scale structure in the Mon R2 cloud. The mean angle of polarization for the complete sample we measured is 158°, which is roughly coincident with the local Galactic magnetic field (155°). The dispersion in the angle of polarization is 33°, similar to that found in the Orion GMC. The dispersion in angle of polarization for stars located along the western side of the three CCD fields is 22°. The CCD fields are bisected by a dense ridge of gas defining the boundary of an expanding gas shell that recent observational results at millimeter wavelengths now reveal dominates the Mon R2 GMC. Our results suggest that the expanding shell has distorted the magnetic field lines extending from the core to the northern gas structure comprising Mon R2.

Subject headings: ISM: individual (Monoceros R2) — ISM: magnetic fields — polarization

1. INTRODUCTION

For some time now it has been suspected that magnetic fields play a major role in determining the mass spectrum of stars formed in molecular clouds. Theoretical models of protostellar evolution in a quiescent environment invoke magnetic fields as one form of cloud suppert and one which has a decisive effect on the minimum stellar mass formed (cf. Shu, Adams, & Lizano 1987; Shu et al. 1988). The magnetic field also might act as an angular momentum damping mechanism—a vital requirement for gravitational collapse and subsequent star formation (Gillis, Mestek, & Paris 1974; Mouschovias 1978). Empirical evidence of the contribution of magnetic fields to the total energetics of molecular clouds comes from analysis of Zeeman splitting of OH absorption and thermal emission lines originating from moderately dense ($n \sim 10^3$ cm^{-3}) cloud cores (Myers & Goodman 1988; Heiles et al. 1991, and references therein). These measurements reveal field strengths as large as one to two orders of magnitude greater than that measured in the diffuse interstellar medium, indicating that magnetic fields are energetically important in dense portions of the ISM.

Measurement of magnetic field strengths in molecular clouds nevertheless remains a formidable task; consequently, efforts are usually focused on determining the *direction* of the magnetic field. We may infer the sky-projected direction of magnetic fields from magnetic alignment of rotating interstellar dust grains. Although slight modifications are apparently in order, the classic Davis & Greenstein (1951) paramagnetic relaxation mechanism is generally assumed to be the correct explanation of the grain alignment phenomenon. Since the grains are anisotropically oriented, starlight shining through cloud will be polarized. Thus, measurements of the polarized far-infrared thermal emission from the dust grains and optical and near-infrared polarization by selective extinction of background stars will give time-averaged direction of the magnetic field (cf. Lee & Draine 1985; Hildebrand 1988). Far-infrared polarimetry is useful for studying high-opacity regions of molecular clouds but can be carried out only above Earth's troposphere. Optical polarimetry has the advantage that it can be accomplished using modest ground-based telescopes, but it has the drawback of being limited to diffuse media and to low-opacity regions ($A_v < 5$) of molecular clouds. Near-infrared polarimetry has been generally limited by the detector technology. With the advent of sensitive large-format CCDs and near-infrared detectors, optical and near-infrared polarimetry is now more widely applicable to the overall molecular cloud environment.

Previous radio studies of the molecular gas in Mon R2 (Kutner & Tucker 1975; Loren 1977; Bally & Lada 1983; Maddalena et al. 1986), as well as recent efforts (Myers-Rice & Lada 1991; Xie 1992), and infrared surveys of the embedded population of stars (Beckwith et al. 1976; Thronson et al. 1980; Hackwell, Grasdalen, & Gehrz 1982) have revealed this cloud to be a kinematically complex region undergoing vigorous high-mass star formation. Analogous to polarimetric studies of dense molecular clouds (cf. Dyck & Lonsdale 1979), there is

[1] NRC Resident Research Associate, Infrared Processing and Analysis Center, Jet Propulsion Laboratory, California Institute of Technology, Pasadena, CA 91125.
[2] Visiting Astronomer, Kitt Peak National Observatory, NOAO, which is operated by the Association of Universities for Research in Astronomy, Inc., under cooperative agreement with the National Science Foundation.
[3] Department of Physics and Astronomy, Northwestern University, Evanston, IL 60208.
[4] Five College Radio Astronomy Observatory.
[5] Jet Propulsion Laboratory, California Institute of Technology, MS 169-506, Pasadena, CA 91109.
[6] National Astronomy and Ionosphere Center, Department of Astronomy, Cornell University, Ithaca, NY 14853.

some evidence that magnetic fields play an important role in relatively high energy environments such as Mon R2. The results of far-infrared polarimetry of Orion A (Novak et al. 1989; Novak, Predmore, & Goldsmith 1990) suggest that the magnetic field possesses a substantial degree of order and has played a role in the formation of massive stars in this GMC. Sato et al. (1988) note that some of the flattened structures seen in the ρ Ophiuchi cloud are consistent with gravitational collapse along the ambient magnetic field. Likewise, optical and infrared polarimetry of the Mon R2 *core* region (Hodapp 1987; Zaritsky et al. 1987; Aspin & Walther 1990) reveal a magnetic field geometry consistent with gravitational contraction primarily along the direction of an energetically important magnetic field. The apparent long axis of the Mon R2 core region is perpendicular to the average magnetic field direction, and the field lines suggest curvature possibly due to contraction along the direction perpendicular to the field. Furthermore, the magnetic field direction is parallel to the long axis of the high-velocity bipolar molecular outflow (cf. Bally & Lada 1983; Xie, Goldsmith, & Patel 1993) centered near the embedded infrared cluster. A field direction–outflow axis coincidence has also been observed in other molecular clouds (Hodapp 1984; Strom et al. 1986). In a related study, Aitken et al. (1993) find that most high-mass protostellar objects possess a magnetic field direction that lies in the plane of their toroidal disks (i.e., perpendicular to the outflow axis). Theoretical modeling of low-mass star formation tends to favor a scenario in which cloud collapse starts along the magnetic field direction, forming flattened structures (cf. Mouschovias 1976; Shu et al. 1987); however, no consistent empirical evidence have thus far been obtained to verify this (e.g., Vrba, Strom, & Strom 1976, 1988; Heyer et al. 1986; Goodman et al. 1990; Klebe & Jones 1990; Goodman et al. 1992). The mixed results underscore the complexity of protostellar evolution in which the gas undergoes stages of gravitational collapse and mass outflow, all the while influenced by cloud rotation and the ambient magnetic field. In addition to local environmental factors, the star formation may also be influenced by large-scale events, such as shock waves from nearby supernova or winds from OB stars. The Mon R2 giant molecular cloud is a prime example. To date, the most extensive view of the complex gas structure of the Mon R2 region comes from the millimeter-wave study of Xie (1992) and Xie & Goldsmith (1994). They found that the large-scale structure of Mon R2 is dominated by a blueshifted (supersonic) expanding shell with a dynamical crossing time of a few million years.

In this paper we present CCD R-band polarimetric observations of stars located behind the Mon R2 giant molecular cloud ($d \sim 850$ pc; Herbst & Racine 1976; Loren 1977). Our goal is to investigate the overall magnetic field geometry in this high-mass star formation region; until recently, it has not been feasible to map magnetic fields throughout an entire GMC. By combining techniques for studying the field in dense regions (infrared polarimetry) with optical CCD polarimetric techniques to measure the magnetic field structure at the largest scales (this study), we may better understand issues related to the ISM and star formation, as well the role of magnetic fields in GMCs in relation to the Galaxy as a whole (Parker instabilities, spiral density waves, etc.). We present the observations, data and calibrations in the following section, including a brief discussion of the new polarimetric technique used in this study. Our method effectively circumvents problems caused by variations in the atmospheric transmission that occur on timescales shorter than the period of modulation of the polarization. The basic technique is to observe the sky through a succession of polarizers, each of which has a hole drilled through its center. By carefully positioning the CCD array, stars located in the center of the field are viewed without any polarizer in the light path. The measured intensities of these stars serve to monitor changes in atmospheric transmission. The effects of these changes are subsequently removed from the polarization results that are obtained for the stars that are observed through the polarizers. In a separate paper (Novak & Jarrett 1994) we discuss in greater detail our polarimetric technique. The results of the polarimetry are presented in § 3, followed in § 4 by a discussion of the magnetic field structure in Mon R2.

2. OBSERVATIONS AND DATA

The polarimetric data collected in this program consist of optical CCD images of fields toward the Mon R2 molecular cloud complex. The observations were carried out over a period of three nights beginning 1992 January 24 using a Tek 2048 CCD camera mounted (f/7.5) to the Kitt Peak National Observatory 0.9 m telescope. A summary of the physical characteristics of the detector as well as the telescope can be found in Schoening et al. (1990).

The detector configuration is as follows. Four linear polarizing filters, with position angles 0°, 90°, 45°, and 135°, were loaded into a rotating filter-wheel assembly. The polarizers are commercially available photographic filters, with one important modification: A small hole of size 9/16 inches (1.4 cm) was drilled out of the center of each Polaroid filter. The effective area of the hole is $\sim$12%–15% of the CCD field. A Cousins R_C broad-band filter, held in a fixed position directly in front of the filter-wheel, was employed in tandem with the Polaroid filters and CCD to complete the polarimetric detector system. With this configuration, roughly 85% of the CCD field is subject to an R-band/Polaroid filter combination, while the remaining $\sim$10%–15% of the field is screened through the R filter alone.

Three CCD fields were imaged in Mon R2 using the R-band and Polaroid filter combination. The field areas were $\sim 23' \times 23'$ each, centered at these locations: (1) $\alpha = 6^h05^m21^s$, $\delta = -6°22'33''$; (2) $6^h04^m36^s$, $-6°05'29''$; and (3) $6^h04^m46^s.2$, $-5°39'51''$ (1950). In addition to the polarimetry data, V, R, and I images were obtained for the Mon R2 fields to provide color information, while fields which included Landolt flux standard stars (Landolt 1983), and known polarized stars were obtained to provide calibration information. The calibrations are described in the following section.

2.1. *Data Reductions*

A series of four or five exposures were taken for each Polaroid orientation, 0°, 90°, 45°, and 135°, giving a total of 16–20 images per field. Each raw CCD image was subject to bias and dark current corrections, flat-field division, cleaned of cosmic-ray hits and cosmetic anomalies, and corrected for atmospheric extinction. IRAF routines were used for these corrections, and the extinction coefficients were checked against mean site values. The average R-band extinction coefficient was determined to be $\sim$0.185, which is roughly a factor of 2 larger than the mean KPNO value averaged over a ten year period or so (G. Jacoby, private communication). This "additional" extinction probably resulted from the tiny ice particles in the upper atmosphere that formed SO_2 gas released from the recent 1991 Mount Pinatubo eruption. Next, the images were corrected for

variations in atmospheric transmission. This correction was determined from stars located in the *center* of the image where the filter hole was aligned with the CCD field; and thus, the intensities were subject to the R-band filter only. In this way we are able to correct for small transmission differences between exposures of the four polarizing filters.

The next step was to perform synthetic aperture photometry for stars located within the portion of the CCD field subject to the polarizing filters. For each star the aperture size was carefully chosen in order to minimize the uncertainties due to Poisson effects. This step is particularly important for our data set since the PSF varies widely across the field of view due to optical aberrations stemming from the large physical size of the Tek 2048 CCD array. The aperture radius varied from 4″ to 8″ depending on the size of the corresponding stellar profile, estimated using an elliptical Gaussian least-squares fit. The background or sky contribution was measured using an annulus of radii 8″–11″ and subtracted from the integrated stellar flux. The precision of the sky-subtracted stellar flux measurement was estimated from the Poisson contribution due to the star and from the variance in the sky flux. The sky-subtracted stellar fluxes of each sequence were then combined into the normalized Stokes parameters, q and u, and weight-averaged to obtain the final estimates of the Stokes parameters, $\bar{q}$ and $\bar{u}$. Here we have followed the conventions of Serkowski (1974). The fluxes were weighted according to the estimated precision in the measurement. In Novak & Jarrett (1994) we describe in detail the method we used to estimate the uncertainties that apply to $\bar{q}$ and $\bar{u}$. Briefly, our method was to use the weighted-standard deviation of the individual measurements of Stokes parameters q and u to determine the uncertainties. However, we modified this procedure somewhat to account for the small number of exposures at each polarization angle. The conversion to the degree, P, and angle, θ, of polarization, and their associated uncertainties, follows in the standard way.

Each star is assigned a V, R, and I magnitude based on the broad-band images, taken at the end of the observing run. From Landolt standards, we determine the $(p-R)$, $(r-R)$, $(V-R)$, and $(V-I)$ color transformation coefficients, where r is the raw R-band magnitude, and p is the raw magnitude of the R plus Polaroid-filter combination. The photometric accuracy of the color transformations is $\sim 10\%$, which is not a major concern since the primary focus of this study is to measure accurate polarimetric fluxes. In addition, the V and I images were not sufficiently deep in order to obtain $V-I$ colors for the faintest R-band program stars.

2.2. *Polarimetry Calibrations*

In order to determine the instrumental polarization, we observed a number of unpolarized stars located in the M67 cluster, as well as one highly polarized source in the L1641 cloud of Orion. A more complete discussion is given in Novak & Jarrett (1994).

The old Galactic cluster M67 serves as an excellent calibration field owing to its close proximity (750 pc; Eggen & Sandage 1964), abundant population, and minimal obscuration (Janes & Smith 1984). The polarizations of these stars have not been independently measured but are probably less than 0.3% (see below). We computed the Stokes parameters for bright stars ($R < 13$) located uniformly throughout the CCD field. On average we measure 0.2% as the degree of polarization. To test the uniformity of the filters/detector combination we divided the CCD field into eight contiguous zones, each of size $\sim 7\farcm7 \times 7\farcm7$. The degree of polarization in each zone is comparable to the ensemble average, and there is no indication of a transmission gradient across the field. We conclude that the upper limit to the instrumental polarization is $<0.3\%$ (Novak & Jarrett 1994). Although we make no correction for this effect in the measured Stokes parameters, we do add 0.3% in quadrature to the estimated Stokes uncertainty ΔP.

As a further check of our methods and detector capabilities, we observed the highly polarized source VSS 185 (Vrba et al. 1988, hereafter VSS) located toward the L1641 molecular cloud. The measured R-band polarization of VSS 185, $7.3\% \pm 0.7\%$, is consistent with the published visual value of VSS, $6.9\% \pm 0.6\%$, within the 1 σ error limit. The angle of polarization, $70° \pm 4°$, is within ~ 2 σ of the VSS value $61° \pm 1°$. We conclude that the methods used in this study to measure linear polarization of stars provide results that are consistent with those measured using standard techniques.

3. RESULTS

Three $23' \times 23'$ CCD fields were observed toward the Mon R2 region. The first field (henceforth, Mon R2 Core) is centered on the dense core of the Mon R2 molecular cloud, and includes as well the powerful bipolar molecular outflow observed by Loren (1977) and Bally & Lada (1983). The second field (Mon R2 NW) lies roughly 17′ north and 12′ west of the core. The third field (Mon R2 NN) lies roughly 42′ north and 8′ west of the core.

In Mon R2 Core we detected ~ 190 stars with S/N ratios $>50:1$. The R-band magnitudes of these stars range from 12 to 18. The bright end was constrained by the dynamic range of the CCD. Within the central 20% of the field (subject only to the R-filter) another half-dozen stars were detected that had expected photometric errors $<1\%$. These stars were used to calibrate against variability in atmospheric transmission. Of the total polarimetric sample, ~ 80 sources had measured linear polarizations accurate to better than 3 σ, or $P/\Delta P \geq 3$. In Mon R2 NW we detected ~ 190 and in Mon R2 NN ~ 250 stars with S/N ratios $>50:1$. Within the central 20% of the NW field another five stars were detected that had expected photometric errors $<1\%$, while seven were detected in the center of the NN field. Of the total polarimetric sample, ~ 95 sources in the Mon R2 NW had measured linear polarizations accurate to better than 3 σ, while ~ 57 were measured with this accuracy in Mon R2 NN.

In order to properly trace the magnetic field structure of the Mon R2 molecular cloud, it is essential that we isolate only starlight which is polarized by clouds in Mon R2. Given the distance of Mon R2 (~ 850 pc) we expect a large fraction of stars in our polarimetric sample to be located in front of the cloud, and thus polarized by the interstellar medium *foreground* to the Mon R2 GMC. However, since the foreground extinction is small, $E(B-V) < 0.27$ (Herbst & Racine 1976), we expect the polarization due to the foreground ISM to be less than 1% or 2%. This value is probably an upper limit given that the Herbst & Racine extinction is an upper limit (determined from R association stars in the Mon R2 cloud) and that VSS measured a foreground polarization component of less than 0.3% for the Orion GMC, which is located in roughly the same area relative to the Galactic disk as Mon R2 (although, it is about half as distant as Mon R2). It should also be noted that mm-wave studies of Mon R2 find no significant clumps of gas foreground or background to the Mon R2 GMC (Xie 1992). Following a procedure similar to that of VSS, we

estimated the foreground interstellar polarization component by first plotting the Stokes parameters for all stars brighter than $R = 17$ with $(V-I)$ colors <2.2. With this brightness limit we expect more than two-thirds of the observed stars to be located in front of the molecular cloud.[7] The color constraint eliminates heavily reddened stars, presumably located behind the molecular cloud. Finally, the "foreground" sample was limited to those stars with measured $\Delta P < 0.7\%$ to eliminate objects with poor Stokes measurements. The results are shown in Figure 1. In Figure 1*a* we plot the Stokes parameters for the entire sample with $\Delta P < 2\%$, and in Figure 1*b*, we show the sample after being culled with the "foreground" criteria. Consistent with our expectation that the foreground polarization is small, most of the stars in Figure 1*b* cluster around the origin in the q-u plane. There are a few stars with polarizations $>1\%$, but this is not unexpected since distant, luminous giants could survive this culling process, and also our sample includes stars with 1 σ errors of up to 0.7%. From Figure 1*b* we estimate the foreground polarization component to be $q = 0.25\% \pm 0.45\%$ and $u = 0.20\% \pm 0.40\%$. The uncertainty in these values is large, due in part to our inability to measure polarizations less than $\sim 0.3\%$ (the estimated uncertainty in the instrumental polarization), which may also be indicative of foreground polarization primarily due to a mixture of low-opacity clouds along the line of sight. We correct our polarimetric sample for the foreground polarization by subtracting the estimated foreground component from the measured (q, u) values of each star. Even though our estimate of the foreground component is poor, this value is still small compared to the overall Stokes uncertainties: the foreground subtraction changes the angle of polarization by $\leq 5°$, typically less than 1 σ of the estimated intrinsic uncertainty in θ.

Accordingly we restrict the foreground polarization corrected sample to only those stars with measured polarizations greater than 1% and $P/\Delta P \geq 3$. The results of the foreground-corrected polarization measurements for these stars are given in Table 1. The coordinate positions are accurate to 10″–15″. The estimated photometric error of the V, R, I photometry is $\sim 10\%$. In Figure 2 we plot the R-band polarization vectors for the Mon R2 Core sources. The E vectors are overlaid on the R-band CCD image of the Mon R2 Core region. The length of the electric vectors is proportional to P. The large circle denotes the area of the field corresponding to the hole in the Polaroid filters; stars located within the encircled area were used only for flux calibration. Also shown in Figure 2 are the I-band and K-band polarization vectors measured by Hodapp (1987) for the central 3′ region of the cloud core (and located within our "hole" area). The Mon R2 bipolar molecular outflow long-axis direction (Bally & Lada 1983) is indicated with arrows directed toward the northwest (blueshifted gas) and southeast (redshifted gas). Likewise, the R-band polarization vectors for the sources located in the Mon R2 NW and NN fields are plotted in Figures 3 and 4, respectively.

3.1. *The Polarization Mechanism*

The goal of this study is to measure the component of starlight polarized by magnetically aligned grains in the Mon R2 molecular cloud. This opertation is complicated by not only the foreground extinction but also the fact that there are two additional components of polarized starlight that are both independent of magnetic fields. We consider two alternative polarization mechanisms: (1) polarization by scattering of starlight from interstellar dust associated with the extended Mon R2 cloud, and (2) intrinsic stellar polarization.

First we consider scattering by dust in Mon R2. With the local young stellar cluster providing the starlight and the dense filamentary gas structures acting as an efficient reflector, the dominant form of polarization is undoubtedly from a scattered light component. Indeed, it is evident from our deep broad-band CCD data that scattered light is abundant in the Mon R2 region. However, it is not likely that the net or integrated polarization we measure for stars includes an appreciable scattered light component. Our method of measuring the polarization of stars relies upon a local background subtraction via aperture photometry. The typical size of a photometry aperture is $\sim 10''$, and the circular annulus used for the sky subtraction extends another 5″ from this boundary. Thus, any scattered light measured in the aperture will exactly cancel the scattered light measured in the local sky annulus, unless there is a strong spatial gradient, over roughly a few arcseconds in the scattered light. If, as we hypothesize, dust grains are mag-

[7] The stellar number densities are estimated from a Galactic stellar distribution model (Jarrett 1992).

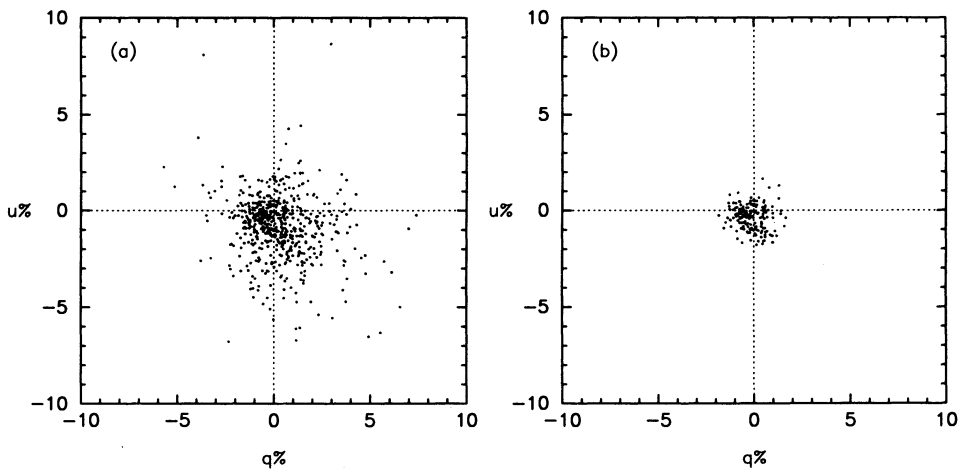

FIG. 1.—Stokes parameters, q and u, corresponding to (*a*) stars with $\Delta P < 2\%$, which effectively represents the entire sample, and (*b*) stars brighter than $R = 17$, $(V-I)$ colors <2.2 amd $\Delta P < 0.7\%$, criteria used to isolate stars located foreground to the Mon R2 cloud.

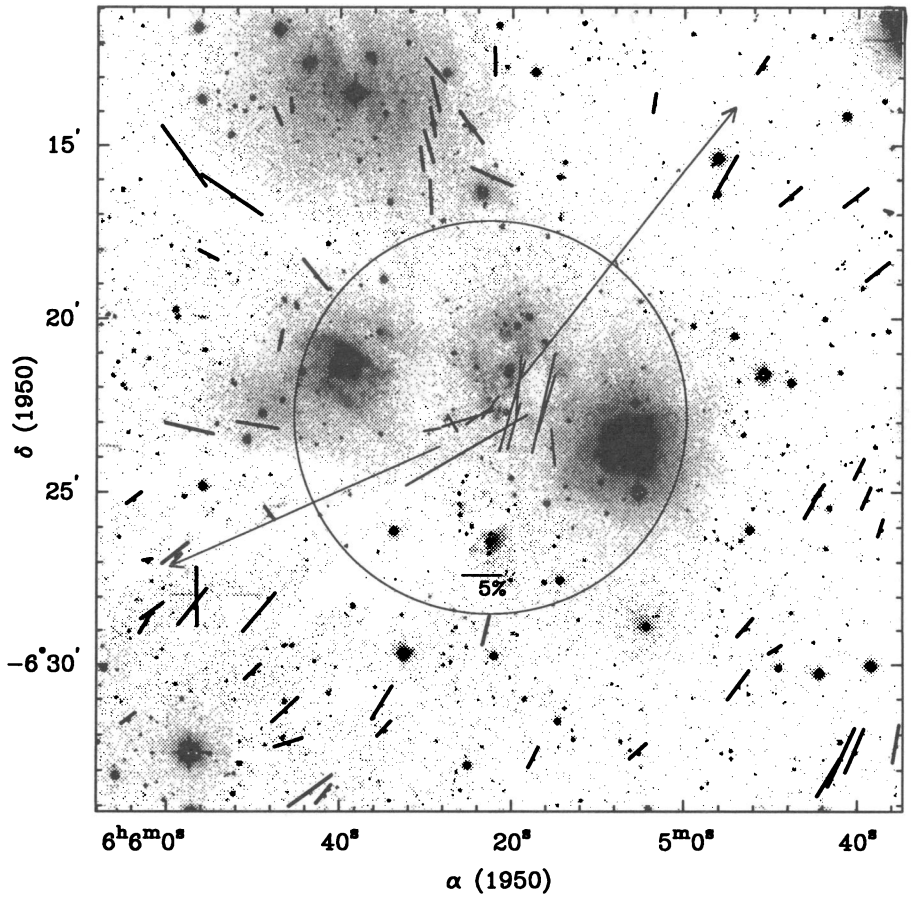

FIG. 2.—*R*-band polarization vectors corresponding to Table 1 sources overlaid on *R*-band CCD image of the Mon R2 Core region. The length of the electric vectors is proportional to *P*(%). The large circle denotes the area of the field corresponding to the hole in the Polaroid filter. The *I*-band and *K*-band polarization vectors (Hodapp 1987) for the central 3′ region of the cloud core are also shown. The Mon R2 bipolar molecular outflow long-axis direction (Bally & Lada 1983) is indicated with arrows directed toward the northwest (blueshifted gas) and southeast (redshifted gas).

netically aligned, then starlight passing through the cloud will be dichroically absorbed by the grains; the resulting polarization can be measured with respect to the local background radiation, irrespective of the Rayleigh-scattered polarized light.

We have argued that our method is insensitive to diffuse-scattered light. Nevertheless, we are still vulnerable to highly polarized light from young stars associated with the star-forming cluster. The source of this polarization is probably due to local scattering from a dusty circumstellar/envelope structure. Given that none of our 3 σ detections are identified with *IRAS* point sources, our observations are probably not sensitive enough to detect very many of these (typically) heavily embedded objects. Next consider intrinsic stellar polarization in field stars. Intrinsic polarizations of up to 1%–2% have been observed in late-type giants (cf. Dyck, Forbes, & Shawl 1971). As in the case of young stellar objects, the polarization mechanism is most likely related to scattering from an anisotropic media associated with the evolved star. Based on the large degree of polarization for the Mon R2 stars (see Table 1), the relative contribution from evolved giants is essentially negligible, or at worst it adds a small dispersion to the measured angle of polarization.

Finally, we expect few of the sources in Table 1 to belong to the stellar population lying foreground to the Mon R2 cloud. As noted above, foreground stars should have small (<1%) polarization since the line-of-sight extinction is most likely less than $1A_v$. Moreover, the extensive polarimetric measurements of Mathewson & Ford (1970) for bright stars near the Monoceros region (and thus representative of the field star population, including nearby stars and distant giants) generally do not show polarizations greater than 1%.

3.2. *Polarization and Visual Extinction*

In order to better understand the relationship between polarization via selective optical extinction of starlight and the intervening, aligned dust grains in the Mon R2 molecular cloud, we construct a polarization-extinction, P versus A_v, relation. Extinction due to the molecular clouds was estimated for the three fields using CO molecular gas column density measurements.

A very good tracer of the dust extinction is the molecular gas column density. The gas column density is typically estimated from CO $J = 1$–0 emission line data. Xie (1992) estimated the visual extinction of the Mon R2 GMC using ^{13}CO column densities. The gas column densities were estimated from ^{12}CO and ^{13}CO (the latter was acquired by Bally, Langer, & Liu 1991) using the LTE method (Dickman 1978). Even though there is a fair amount of uncertainty in the absolute conversion to A_v, the relative extinction should be reliable for moderate to high opacities.

The resultant visual extinction values range from 1 to 20 mag. The relative extinction values corresponding to the stars

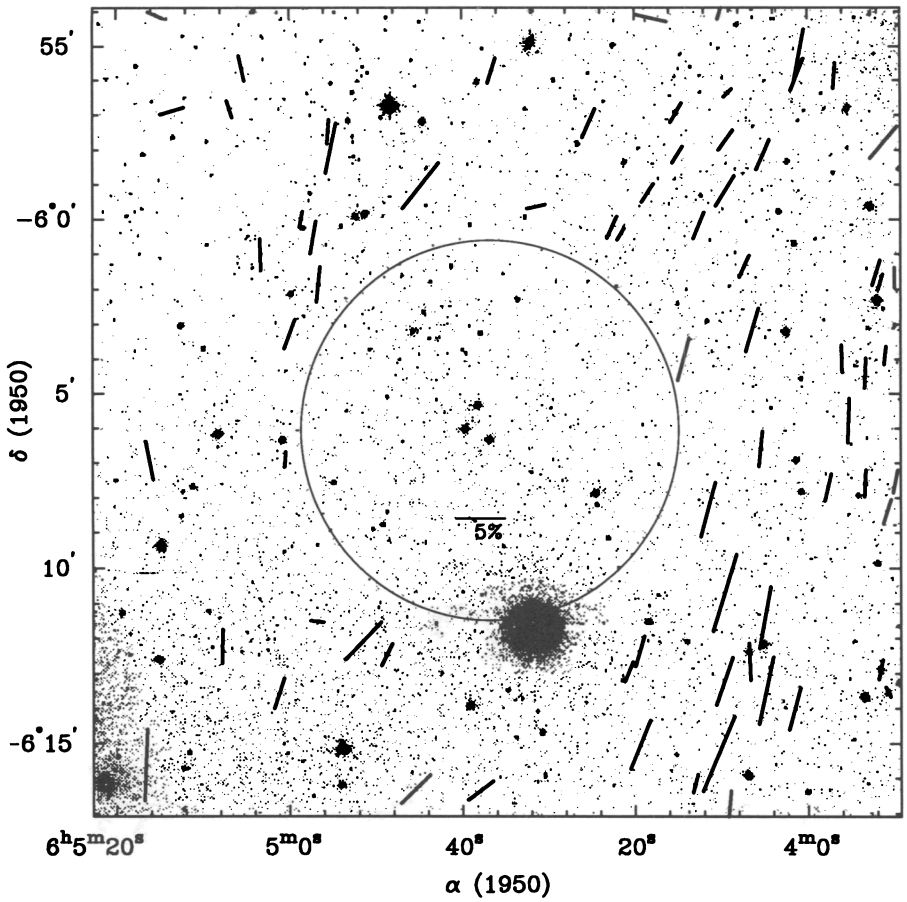

FIG. 3.—*R*-band polarization vectors corresponding to Table 1 sources overlaid on *R*-band CCD image of the Mon R2 NW region. The symbols used are described in Fig. 2.

with 3 σ polarizations are given in the last column of Table 1. Figure 5 shows the P versus A_v relationship for the Mon R2 stars in Table 1. Also shown in Figure 5 is the P/A ratio adapted from the Serkowski, Mathewson, & Ford (1975) relation: $P_{max}(\%) \leq 9.0E(B-V)$, which represents the empirical upper limit observed for stars in the field (i.e., corresponding to the diffuse interstellar medium). Here we assume a value of 3.2 for the ratio to total selective extinction and use Serkowski's $P(\lambda)$ versus P_{max} law, relating P_v to P_R, where we assume λ_{max} is near λ_v (see also Hiltner 1956; Clayton & Carelli 1988; Klebe & Jones 1990). Although there is significant scatter in the P to A relationship in Figure 5, there are no points for which the ratio has a value much greater than 2.9, suggesting that the grain alignment mechanism in Mon R2 is probably similar to that functioning in the general interstellar medium. The overall P-A trend, although very weak, is that of increasing polarization with extinction, in which the peak polarization occurs for $A_v \sim 6$. For heavily obscured regions of the Mon R2 fields, the polarization appears to be decreasing or at least remain flat with increasing extinction. The scatter in the relation is also increasing with opacity. These results are similar to those found in other polarimetric studies of molecular clouds (cf. Vrba et al. 1976; Klebe & Jones 1990). It has been hypothesized that a flattening in the P-A_v relation is related to the dust grains themselves; for dense regions the *efficiency* of polarization is lower relative to more diffuse areas of the cloud. Clayton & Cardelli (1988), for example, have argued that the flattening seen in the P-A_v relation at large A_v may be due to a grain population with increasing physical sizes via coagulation of small dust grains—the signature being an increasing ratio of total-to-selective extinction R_v—which is less efficient at dichroically absorbing starlight.

In a related issue, Jones (1989) and Jones, Klebe, & Dickey (1992), among others, have demonstrated with numerical models that the degree of polarization, as well as the dispersion in the direction of polarization (Myers & Goodman 1991), may be influenced primarily by the line-of-sight column density of the polarizing dust grains (which Jones et al. 1992 assume are in perfect alignment) and magnetic field geometry. An important assumption that these models adopt is that the magnetic field is composed of a uniform and random component. The basic idea is that as the starlight passes through the molecular cloud it encounters clumps of gas, each of which is coupled to a nonuniform (or random) component of the ambient magnetic field. Thus, there is a characteristic scale length corresponding to an opacity at which the random component of the magnetic field decorrelates. In this way, the large scatter seen in Figure 5 may be related to a changing magnetic field geometry as the *line-of-sight* extinction increases, where the decorrelation opacity is of order $2A_v$. In summary, we have suggested alternative mechanisms that might explain the observed weak correlation between P and A_v. In previous sections, we have argued that our measurements determine magnetic field directions within the Mon R2 cloud, with the qualification that

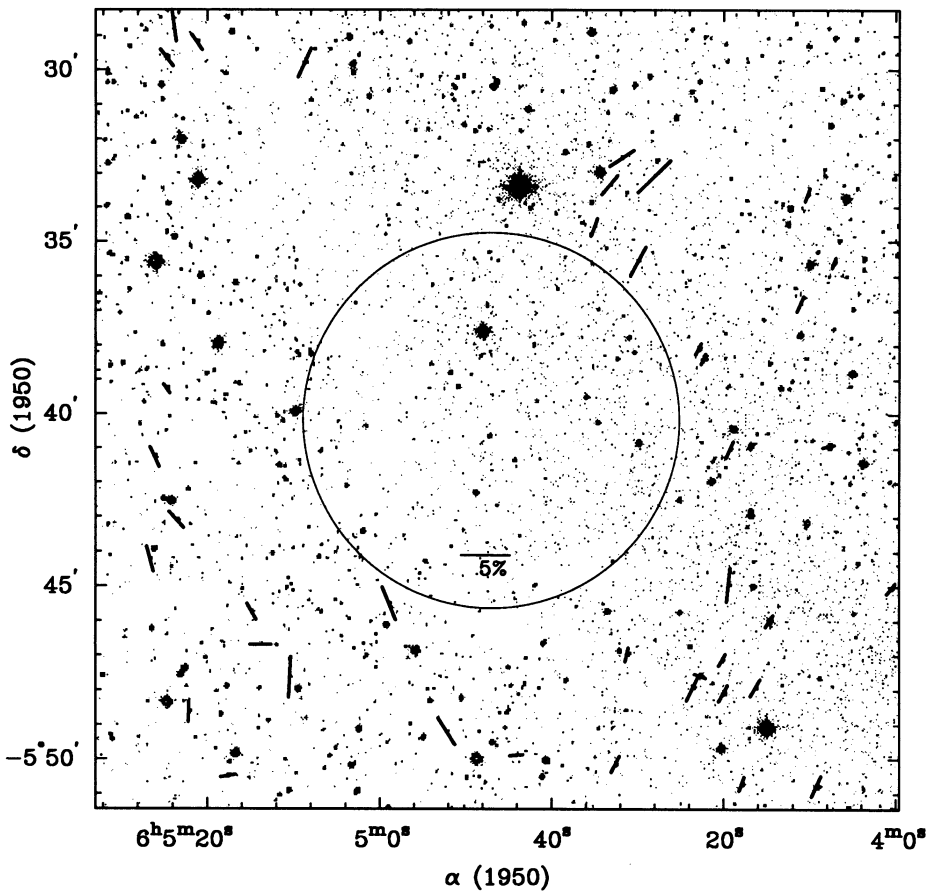

FIG. 4.—*R*-band polarization vectors corresponding to Table 1 sources overlaid on *R*-band CCD image of the Mon R2 NN region. The symbols used are described in Fig. 2.

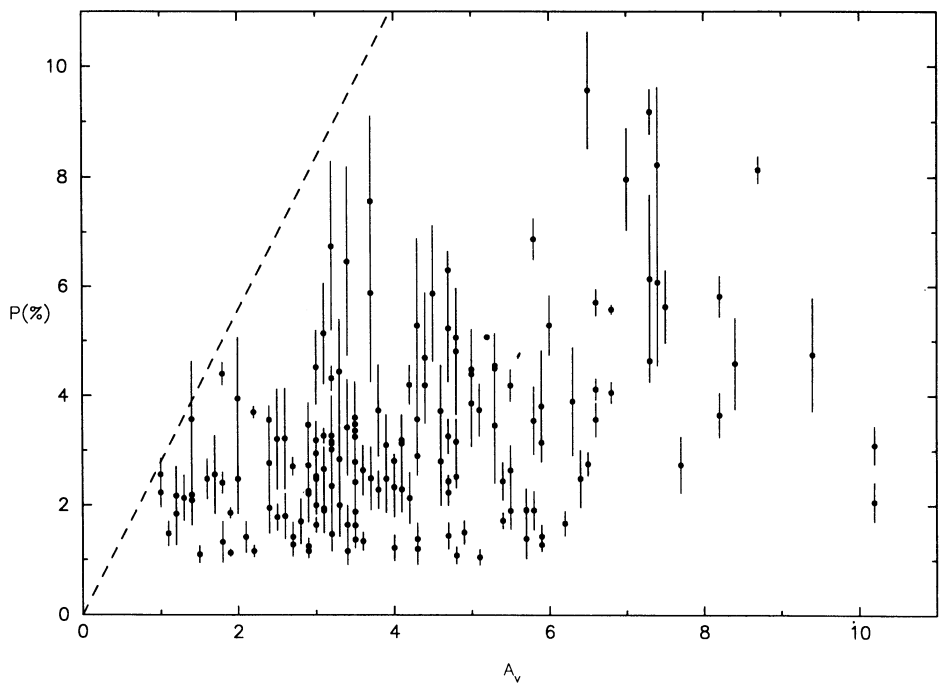

FIG. 5.—Percentage polarization vs. visual extinction for stars observed through the Mon R2 cloud (Table 1). Also indicated is the *P*/*A* upper limit observed for field stars observed through diffuse interstellar clouds.

TABLE 1

MONOCEROS R2 LINEAR POLARIZATION MEASUREMENTS FOR STARS WITH $P > 1\%$ AND $P/\Delta P \geq 3$

α (1950) hh mm ss	δ (1950) dd mm ss	V	V-R	R-I	P %	ΔP %	θ°	σ(θ)	A(V)
06 05 40.4	-6 33 40	16.1	1.2	0.9	3.0	0.5	140.5	4.8	3.2
06 05 42.0	-6 33 35	18.0	...	1.2	6.7	1.9	125.6	5.8	3.2
06 04 41.9	-6 33 12	14.3	1.8	1.4	5.6	0.3	148.3	0.5	6.8
06 05 16.1	-6 32 38	16.8	...	1.2	2.8	0.9	152.7	8.4	4.6
06 04 40.4	-6 32 38	17.4	...	1.5	8.0	1.1	154.8	3.4	7.0
06 05 3.9	-6 32 28	15.4	1.0	0.9	2.8	0.4	130.6	2.0	6.5
06 04 38.9	-6 32 27	15.8	...	1.4	5.8	0.5	156.1	1.8	8.2
06 04 34.1	-6 32 15	16.2	...	...	4.6	0.5	170.1	2.2	7.3
06 05 44.5	-6 32 13	17.3	...	0.9	3.7	1.0	106.9	5.4	3.8
06 05 33.4	-6 31 50	15.4	1.2	1.0	2.5	0.4	137.0	3.1	4.8
06 06 3.1	-6 31 32	15.7	0.8	0.6	2.2	0.6	127.6	7.3	2.9
06 05 44.9	-6 31 18	17.3	...	0.9	4.4	1.0	132.5	3.1	3.3
06 05 33.7	-6 31 6	17.5	...	1.0	4.8	1.2	147.9	6.2	4.8
06 04 52.3	-6 30 36	16.8	...	0.9	4.6	0.7	143.6	3.3	5.3
06 05 48.7	-6 30 13	16.7	0.9	0.8	2.7	0.7	133.1	1.9	2.9
06 04 48.1	-6 29 34	16.3	1.2	0.9	1.9	0.5	123.2	4.0	5.7
06 05 21.6	-6 29 1	16.7	...	1.3	3.9	0.8	167.0	5.2	5.0
06 04 51.6	-6 28 55	16.0	1.5	1.4	3.1	0.4	139.8	2.5	10.2
06 06 1.0	-6 28 46	17.3	...	0.8	3.2	1.0	149.8	8.0	3.5
06 05 47.9	-6 28 28	17.7	...	1.0	6.5	1.8	140.9	10.0	3.4
06 06 0.3	-6 28 25	16.3	0.9	0.8	3.5	0.6	126.6	4.8	3.5
06 05 55.7	-6 28 18	17.9	...	0.9	5.9	1.6	142.6	6.6	3.7
06 05 55.2	-6 28 0	17.6	...	0.8	7.6	1.6	0.6	6.1	3.7
06 06 0.8	-6 26 55	15.4	1.3	1.4	1.2	0.4	99.1	5.5	3.4
06 05 57.7	-6 26 44	15.2	1.6	1.5	4.2	0.4	128.8	2.4	5.5
06 04 35.9	-6 26 0	15.6	...	...	2.2	0.4	162.6	2.8	4.7
06 05 46.8	-6 25 36	15.4	1.3	1.1	2.1	0.5	37.9	5.4	10.2
06 04 43.9	-6 25 23	16.5	...	1.4	3.7	0.6	149.1	3.5	8.2
06 06 2.4	-6 25 10	16.3	...	1.7	2.3	0.6	127.2	7.9	4.0
06 04 37.5	-6 25 10	16.4	1.2	1.0	2.8	0.7	155.6	6.0	3.3
06 04 43.0	-6 24 60	15.4	1.3	1.1	2.4	0.4	144.3	5.1	5.4
06 04 38.3	-6 24 20	16.6	1.2	1.0	2.8	0.7	153.1	6.3	2.4
06 05 56.0	-6 23 10	18.0	...	1.1	6.1	1.9	77.2	7.5	7.3
06 05 48.2	-6 23 5	18.0	...	1.1	5.2	1.8	80.9	7.1	4.6
06 05 45.5	-6 20 37	16.3	...	1.5	2.5	0.6	168.5	7.4	6.4
06 05 41.5	-6 18 42	16.6	0.9	0.9	4.8	1.1	39.4	8.1	9.4
06 04 36.2	-6 18 38	16.5	...	1.2	3.7	0.6	128.0	3.7	5.1
06 05 53.9	-6 18 10	16.1	1.2	1.1	2.6	0.5	61.9	5.6	5.5
06 04 35.0	-6 16 54	14.9	...	...	1.1	0.3	75.1	3.0	4.8
06 04 38.8	-6 16 30	16.6	...	1.5	3.8	1.0	127.2	9.8	5.9
06 05 28.1	-6 16 30	16.0	1.7	1.4	4.2	0.5	3.2	3.6	4.4
06 04 46.4	-6 16 28	15.5	2.1	1.7	3.6	0.4	130.2	2.2	6.6
06 05 51.2	-6 16 26	16.4	...	1.4	9.2	0.5	56.2	1.0	7.3
06 05 21.0	-6 15 55	17.3	...	1.5	5.6	1.0	66.0	3.4	7.5
06 04 53.9	-6 15 54	18.1	...	1.6	6.1	2.0	150.9	7.4	7.4
06 05 29.1	-6 15 22	16.8	...	1.2	3.1	0.9	7.1	8.6	3.2
06 05 56.7	-6 15 19	16.8	...	1.9	9.6	1.1	35.5	4.1	6.5
06 05 28.3	-6 15 1	15.9	1.4	1.2	4.3	0.4	15.9	1.2	3.2
06 05 23.4	-6 14 27	13.8	1.0	0.9	5.1	0.3	36.1	0.2	5.2
06 05 27.9	-6 14 18	13.8	0.9	0.8	3.7	0.3	10.1	0.7	2.2
06 05 45.9	-6 14 8	15.5	1.3	1.1	2.4	0.4	23.9	2.1	1.8
06 05 44.3	-6 13 48	14.9	1.5	1.3	1.9	0.3	0.5	1.7	1.9
06 05 2.1	-6 13 44	16.6	0.9	0.9	2.5	0.7	170.7	7.0	3.0
06 05 27.6	-6 13 29	15.7	1.0	1.0	4.4	0.4	13.4	1.5	1.8
06 05 27.6	-6 12 48	16.7	...	1.2	4.0	1.1	39.3	7.8	2.0
06 04 49.7	-6 12 38	14.0	1.6	1.4	2.4	0.3	147.2	1.2	4.7
06 05 20.7	-6 12 31	17.5	...	1.1	3.5	1.1	0.9	10.5	5.3
06 04 9.1	-6 16 55	16.4	...	...	4.1	0.4	174.6	1.2	6.8
06 04 37.9	-6 16 21	16.6	1.9	1.5	3.2	0.4	126.4	2.5	5.9
06 04 45.5	-6 16 18	15.6	2.1	1.7	4.1	0.4	133.7	1.6	6.6
06 04 13.0	-6 16 9	15.6	1.4	1.2	1.9	0.4	165.2	3.2	5.7
06 04 19.4	-6 15 2	17.2	1.1	1.2	5.3	0.6	157.7	2.9	6.0
06 04 1.5	-6 14 0	16.8	1.8	1.5	4.4	0.5	165.0	2.4	5.0
06 05 1.2	-6 13 34	16.6	0.9	0.9	3.2	0.4	162.0	2.9	3.0
06 03 50.8	-6 13 32	14.4	0.6	0.6	1.1	0.3	26.1	1.5	1.9
06 04 4.8	-6 13 29	16.8	1.5	1.4	6.9	0.5	167.9	1.5	5.8
06 04 9.7	-6 13 13	17.1	1.3	1.0	5.1	0.5	160.8	1.8	4.8
06 04 20.7	-6 12 57	17.4	1.1	0.9	2.1	0.6	157.5	6.2	4.2
06 04 6.7	-6 12 40	18.2	...	...	3.7	1.2	2.5	2.5	4.6
06 04 48.8	-6 12 28	14.0	1.6	1.4	2.4	0.3	153.2	1.3	4.7
06 04 19.5	-6 12 22	17.0	1.0	1.0	3.2	0.5	163.2	4.3	4.8
06 05 7.8	-6 12 13	18.1	...	...	3.4	1.1	179.4	8.7	3.4
06 04 51.5	-6 12 5	18.2	...	1.6	5.2	1.2	135.8	5.4	4.7
06 04 56.8	-6 11 31	15.8	1.4	1.6	1.3	0.3	83.3	2.5	3.6
06 04 5.0	-6 11 24	16.7	1.3	1.4	6.3	0.4	169.5	1.2	4.7
06 04 9.6	-6 10 42	16.6	2.3	1.9	8.1	0.4	162.8	0.8	8.7
06 03 50.9	-6 08 24	16.2	1.3	1.2	2.6	0.4	162.2	3.3	1.0
06 04 11.5	-6 08 20	15.9	1.8	1.6	5.7	0.4	164.9	0.9	6.6
06 03 57.7	-6 07 42	15.5	1.4	1.2	2.8	0.3	167.2	1.0	4.0
06 03 53.4	-6 07 35	15.1	0.9	0.8	2.7	0.3	177.7	0.7	2.7
06 03 49.9	-6 07 31	17.2	1.2	0.8	2.3	0.6	168.8	6.3	3.2
06 05 16.2	-6 06 55	17.8	...	1.3	3.9	1.0	11.1	7.7	6.3
06 05 0.5	-6 06 54	17.1	1.4	1.4	1.6	0.5	175.1	8.1	4.6
06 04 5.4	-6 06 35	17.5	1.4	1.2	3.6	0.7	173.9	3.9	3.5
06 03 55.3	-6 05 46	17.5	2.2	1.5	4.5	0.7	177.8	5.2	5.3
06 03 53.4	-6 04 24	17.6	2.6	1.5	3.1	0.8	177.6	5.1	3.9
06 04 14.4	-6 04 1	18.2	...	...	4.5	1.2	164.9	5.2	5.0
06 03 56.1	-6 03 59	16.6	1.5	1.3	2.8	0.8	1.4	1.4	3.5
06 03 51.1	-6 03 54	16.9	0.9	0.9	1.8	0.5	173.3	7.2	2.6
06 05 0.0	-6 03 17	17.3	1.6	1.2	3.1	0.6	159.9	3.6	4.1
06 04 6.4	-6 03 10	17.2	1.0	1.0	4.5	0.7	163.6	4.7	3.0
06 04 56.7	-6 01 52	15.5	1.7	1.4	3.6	0.4	174.2	1.3	2.4
06 03 51.7	-6 01 48	15.6	1.0	0.9	1.6	0.3	163.0	2.3	3.0
06 03 50.0	-6 01 40	17.3	1.1	1.0	2.0	0.6	179.6	5.5	3.3
06 03 52.1	-6 01 32	17.4	1.5	1.0	2.5	0.7	160.5	7.4	3.0
06 04 7.4	-6 01 21	17.1	1.7	1.2	2.3	0.5	155.1	5.3	4.1
06 05 3.4	-6 01 1	17.8	1.0	1.0	3.2	0.9	1.7	8.2	3.2
06 04 57.3	-6 00 32	17.6	1.3	1.0	3.4	0.8	170.6	6.8	3.5
06 04 21.6	-6 00 25	15.5	1.0	0.8	1.4	0.3	149.3	3.5	3.5
06 04 22.7	-6 00 14	16.4	1.0	0.9	2.4	0.4	155.8	2.8	3.5
06 04 12.6	-6 00 11	17.6	1.0	0.9	2.9	1.0	157.7	9.2	4.3
06 04 58.7	-6 00 01	5.3	1.6	1.2	1.6	0.3	170.1	2.8	3.5
06 04 31.4	-5 59 38	16.7	1.1	1.3	1.9	0.5	102.2	6.3	5.8
06 04 18.5	-5 59 14	17.1	1.0	0.9	2.2	0.6	147.4	8.6	1.4
06 04 9.5	-5 59 11	17.5	1.3	1.1	3.5	0.7	148.1	5.6	5.8
06 04 44.8	-5 59 2	18.2	1.0	1.4	5.9	1.3	141.6	7.8	4.5
06 04 15.1	-5 58 8	17.2	1.1	1.0	2.0	0.6	147.9	5.3	2.4
06 04 5.2	-5 58 8	16.6	1.0	1.1	3.3	0.4	156.1	1.9	3.2
06 04 55.2	-5 57 57	18.2	...	...	5.1	1.2	168.2	5.2	3.1
06 03 51.3	-5 57 47	17.6	...	1.9	4.2	0.8	139.7	2.5	4.2
06 04 9.5	-5 57 43	17.7	1.9	1.2	2.5	0.8	143.8	6.8	2.0
06 04 55.5	-5 57 29	16.8	1.1	0.8	2.5	0.5	175.4	3.8	1.6
06 04 25.3	-5 57 14	17.0	1.2	1.3	3.2	0.6	155.9	4.1	4.1
06 04 15.2	-5 56 56	14.2	1.0	0.9	2.3	0.3	150.1	1.2	2.9
06 05 13.6	-5 56 53	17.6	1.2	1.1	2.5	0.8	106.5	6.4	3.7
06 05 13.6	-5 56 53	17.6	1.2	1.1	2.5	0.8	106.5	6.4	3.7
06 05 6.9	-5 56 50	15.8	0.9	0.9	1.8	0.4	17.4	3.8	2.5

these magnetic field directions are projected onto the plane of the sky and averaged along the line of sight to each star. Finally the P-A_v relation in Mon R2 implies that we cannot be certain which density regimes within Mon R2 are being sampled by our measurements.

3.3. *General Features in the Polarization Field*

In this section we discuss the main features that are evident in our data. For clarity, in Figure 6 we combine the $\boldsymbol{E}$ vectors for the three polarimetric fields, Core, NW, and NN (denoted by large boxes). Also shown in Figure 6 is a gray-scale rendering of the ^{12}CO $J = 1$–0 peak antenna temperature for the Mon R2 core and vicinity. In Figure 7 we show the angle of polarization distributions for the three individual fields and the combined ("all") field result. The histograms are plotted for θ between $90° \pm 90°$. The peak in the combined distribution occurs at a position angle of about 160°. For the remaining analysis we compute θ between $160° \pm 90°$. Using the convention of Myers & Goodman (1991) in which the dispersion in the angle of polarization is measured by fitting a Gaussian to

TABLE 1—*Continued*

α (1950) hh mm ss	δ (1950) dd mm ss	V	V-R	R-I	P %	ΔP %	θ°	σ(θ)	A(V)
06 04 9.2	-5 56 22	15.2	1.0	0.9	1.2	0.3	135.1	3.3	2.2
06 03 56.9	-5 55 52	17.8	1.3	1.4	2.7	0.9	176.0	3.8	3.1
06 04 1.2	-5 55 50	18.1	...	...	3.6	1.1	158.7	5.2	4.3
06 04 36.6	-5 55 43	17.1	1.5	1.4	2.7	0.6	162.7	5.7	7.7
06 05 5.6	-5 55 39	17.3	1.1	0.9	2.6	0.6	12.2	6.1	3.6
06 04 1.0	-5 55 15	18.5	...	...	5.3	1.6	169.3	10.4	4.3
06 04 18.0	-5 54 11	18.0	...	1.4	3.2	1.0	77.1	9.1	2.6
06 05 15.5	-5 54 6	16.0	1.1	0.8	1.6	0.5	66.3	6.0	3.4
06 04 10.1	-5 54 2	16.4	1.3	0.9	1.3	0.4	163.8	4.7	2.7
06 05 16.7	-6 15 37	18.0	...	...	7.2	1.5	177.8	2.1	13.1
06 04 10.3	-6 15 18	17.5	2.2	1.6	8.2	1.4	157.0	5.0	7.4
06 03 51.7	-6 12 53	13.4	1.4	1.2	2.0	0.3	168.1	2.7	3.0
06 04 9.2	-5 50 46	13.5	1.1	1.0	2.3	0.4	155.5	4.5	3.8
06 04 17.9	-5 50 43	14.9	0.8	0.8	1.5	0.4	160.5	5.4	3.2
06 05 17.6	-5 50 29	15.1	1.1	1.1	1.5	0.3	100.1	3.0	4.9
06 04 32.6	-5 50 9	15.0	1.2	1.1	1.8	0.4	152.7	5.5	7.7
06 04 44.1	-5 49 53	15.4	1.0	0.8	1.3	0.4	95.0	6.6	1.8
06 04 52.2	-5 49 12	16.8	...	0.8	3.2	0.9	31.7	8.5	2.5
06 05 22.1	-5 48 38	15.2	...	1.3	2.1	0.3	177.8	3.3	1.4
06 04 20.0	-5 48 5	14.1	0.9	0.9	1.9	0.4	151.5	6.6	3.5
06 04 16.3	-5 47 56	15.3	1.0	0.9	1.9	0.5	149.8	6.4	3.1
06 04 23.5	-5 47 55	14.5	1.8	1.5	2.9	0.4	153.7	3.5	4.3
06 05 10.4	-5 47 38	17.3	...	0.7	4.1	1.4	176.9	3.6	1.6
06 04 22.7	-5 47 35	13.4	0.5	0.5	1.2	0.3	69.6	6.4	4.3
06 04 20.2	-5 47 7	15.1	0.8	0.8	1.4	0.3	150.4	5.2	4.3
06 04 31.2	-5 46 58	15.3	0.8	0.7	1.4	0.3	166.0	3.9	4.7
06 05 13.8	-5 46 41	16.5	...	0.7	2.1	0.7	89.3	7.1	1.3
06 04 14.7	-5 45 59	12.6	1.0	0.9	1.5	0.3	147.2	4.8	1.1
06 05 14.8	-5 45 44	16.0	0.7	0.7	1.8	0.6	29.4	7.0	1.2
06 04 58.9	-5 45 30	16.9	...	0.6	3.6	1.1	22.3	8.4	1.4
06 04 0.5	-5 45 3	15.4	0.8	0.8	1.4	0.4	141.0	7.3	2.1
06 04 19.4	-5 44 56	15.7	1.0	1.0	3.5	0.4	174.3	1.8	2.9
06 05 26.6	-5 44 13	16.5	...	1.2	2.6	0.7	14.6	8.3	1.7
06 05 26.0	-5 41 16	14.9	0.8	0.7	2.2	0.3	24.5	3.4	1.0
06 04 19.3	-5 41 2	16.1	0.9	0.8	1.9	0.5	156.5	5.9	3.1
06 04 7.8	-5 40 55	12.9	2.5	...	1.2	0.3	102.6	4.8	4.0
06 05 24.6	-5 39 17	14.5	0.6	0.6	1.1	0.4	34.2	8.9	1.4
06 04 22.3	-5 38 23	13.2	1.0	0.9	1.2	0.3	155.3	3.1	2.9
06 04 22.9	-5 38 6	13.8	0.4	0.5	1.2	0.3	153.7	3.4	2.9
06 04 11.1	-5 36 47	15.9	0.9	0.8	1.7	0.5	155.8	6.9	2.8
06 04 7.2	-5 35 37	14.3	0.5	0.5	1.1	0.3	160.5	3.8	1.5
06 04 29.9	-5 35 34	15.7	1.2	1.1	3.3	0.4	151.5	1.1	3.1
06 04 35.0	-5 34 35	16.1	0.7	0.7	1.9	0.5	160.2	5.2	5.5
06 04 10.3	-5 33 37	15.5	0.6	0.6	1.4	0.4	159.9	5.1	2.7
06 04 33.2	-5 33 20	16.2	0.8	0.8	2.5	0.6	140.5	4.2	3.9
06 04 28.1	-5 33 5	17.4	...	1.1	4.7	1.5	134.8	8.1	4.4
06 04 31.8	-5 32 33	16.0	...	0.7	3.0	0.5	123.4	3.3	3.0
06 05 8.7	-5 29 47	14.3	...	2.0	3.3	0.4	155.9	2.8	4.7
06 05 24.6	-5 29 38	14.2	0.9	0.7	2.1	0.4	36.8	5.6	4.2
06 05 21.1	-5 29 11	15.9	...	0.8	1.9	0.5	34.6	6.4	8.7
06 05 23.9	-5 28 31	17.0	...	0.7	4.6	1.0	7.8	5.9	8.4
06 05 23.5	-5 43 6	15.8	...	0.9	2.2	0.6	42.3	9.1	1.2

NOTES.—The coordinate positions are accurate to 10″–15″. The estimated photometric errors of the (V, R_C, I_C) photometry is ~10%. The degree of polarization, P, and its uncertainty, ΔP, are expressed as percentages. The angle of polarization, θ, and its uncertainty, $\sigma(\theta)$, are expressed in degrees counterclockwise from position angle 0° (north). The visual extinction, $A(V)$, is estimated from the molecular gas column density in the Mon R2 GMC.

the distribution of polarization angle we find that $\bar{\theta}_E = 159° \pm 1°$ and $s = 0.37 \pm 0.01$ for the combined fields (Fig. 8*a*; Gaussian fit is denoted by the dotted line), where $\bar{\theta}_E$ is the Gaussian center and s is its 1 σ width (in radians). Note that we have fitted only the Gaussian-like feature in the distribution, when in fact it is clear that the distribution has non-Gaussian side "wings." The statistical mean in the distribution is 158° and the standard deviation is 33°. In contrast to these results, it is apparent that in the western half of each of the three fields (see Fig. 6) there is a substantial degree of uniformity in the projected direction of the magnetic field. Figure 8*b* shows the distribution of the position angles for the data set consisting of the western halves of the three fields. A Gaussian least-squares fit yields $\bar{\theta}_E = 158° \pm 1°$ and $s = 0.24 \pm 0.01$, while the statistical mean is 157° with a standard deviation of 22°, which we point out is roughly coincident with the Galactic plane, at ~155°.

In the eastern halves of the three fields, the directions vary much more than the western halves. Even in the eastern halves, however, some order is apparent. The southeastern quadrant of the Core field and much of the eastern half of the NW field show continuity with the adjacent portions of the western halves of these fields (see Fig. 6). However, most of the data for the eastern halves show position angles that are very different from the position angles that characterize the western halves of the fields. The northeastern quadrant of the Mon R2 Core field is perhaps the most dramatically discordant example, with large values of the degree of polarization, and position angles approximately orthogonal to those seen in western halves (see Fig. 7 "core").

Smaller scale maps of the magnetic field in the core of Mon R2 have been made by Zaritsky et al. (1987), who measured R-band polarization within a 9′ × 9′ region approximately centered on the core, and Hodapp (1987), who mapped the I-band and K-band polarization of the central core of Mon R2 (the polarization vectors are shown in Fig. 2). Hodapp uses his data to draw a number of conclusions about the role of the magnetic field in Mon R2. Specifically, he argues that the direction of the minor axis of the cloud, the rotational axis, and the average magnetic field direction are all coincident, and that the overall picture is consistent with simple theoretical scenarios of magnetically diluted gravitational contraction. Hodapp further notes that the bipolar outflow from the core of Mon R2 follows the magnetic field lines.

Our data sample a much larger region than was mapped by either of the two polarization studies mentioned above. At first glance, our results seem to support the arguments of Hodapp. This is because (*a*) they show that the inferences made by Hodapp concerning the large-scale field orientation hold true as one extends the field lines out from the small region he mapped to the larger region encompassed by our Core field (see Figs. 2 and 6), and (*b*) this NW-SE orientation is preserved even on the largest scales, if one considers only the western halves of the fields. However, the results we have obtained in the northeast quadrant of the Core field do not fit in with Hodapp's picture of a collapsing cloud core in a uniform magnetic field. It seems that the field geometry in Mon R2 is sufficiently disturbed (at least near the core) to make it very difficult for one to convincingly explain isolated features in the magnetic field by analogies to simple theoretical models that were developed from studies of gravitational collapse in a uniform magnetic field. As we will show below, there is some evidence that a large-scale shock wave has substantially influenced the magnetic field geometry in Mon R2.

Previously we made a small correction to our measured polarizations to account for the effects of foreground material. While there is some uncertainty in this correction, we argue that the effects of this uncertainty on our data are reasonably small. Thus, we believe that most of the features in our polarization map are due to magnetic alignment of dust grains in the Monoceros R2 giant molecular cloud. For any given feature, however, it is difficult to eliminate the possibility that the polarization is due to foreground material. Because we believe that it is likely, however, that the foreground contribution does *not* have a significant effect on the gross features that we have

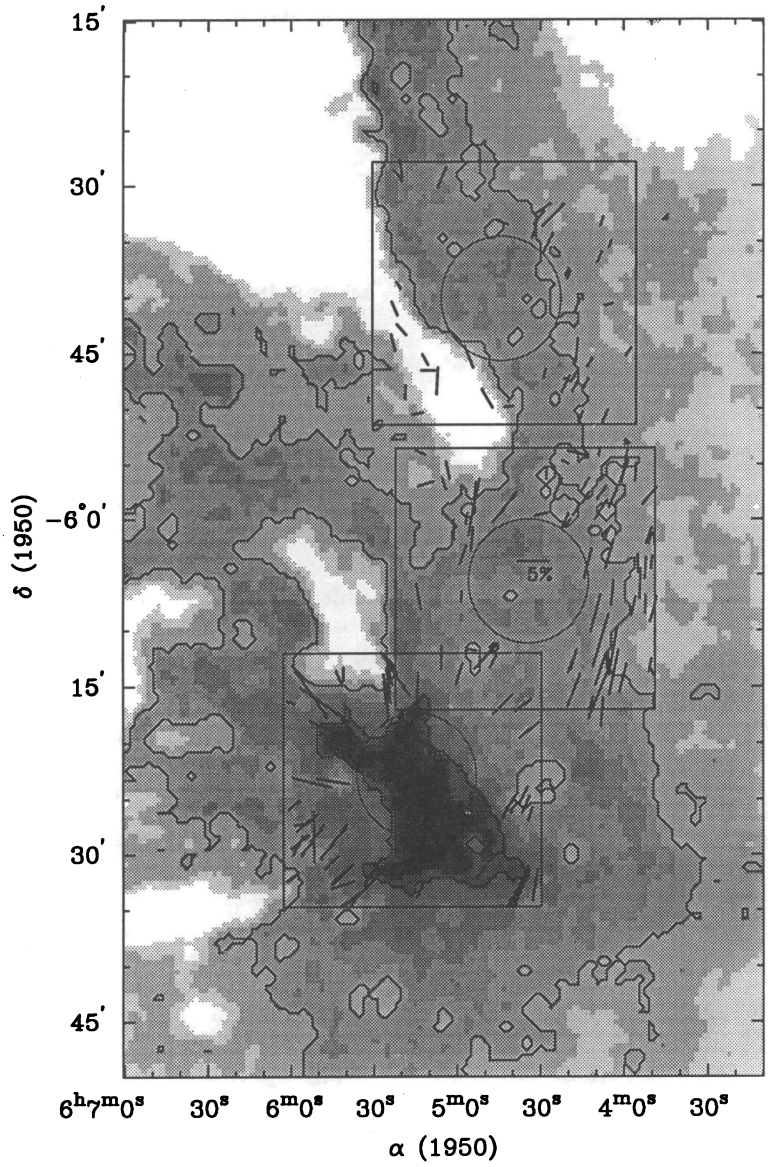

FIG. 6.—^{12}CO $J = 1$–0 peak antenna temperature for the Mon R2 core and vicinity. The temperature (and gray scale) ranges from 1 to 15 K; contour levels correspond to 4 and 8 K. The gray scale is overlaid by the polarization vectors of the three fields observed in this study, Core, NW, and NN regions, from south to north.

discussed in this section, we will proceed, in the following section, to discuss these gross features under the assumption that they *do* represent magnetic field geometry in the Mon R2 cloud. Finally, it must be emphasized that polarimetric measurements and subsequent interpretation of the magnetic field structure is limited to the plane of the sky.

4. DISCUSSION

It is evident that the inferred magnetic field structure of Mon R2 is far from simple. Polarimetry of the three CCD fields presented in this work reveals an overall structure common to each field but with significant differences. These nonuniformities are possibly related both to small-scale changes in the gas associated with massive star formation and to the large-scale alteration of the cloud geometry by a shock-compressed gas shell. For the sake of clarity, we consider these issues separately.

4.1. *Small-Scale Field Structure*

The "Core" region—the location of one of the most energetic and complex bipolar outflows observed in molecular clouds and the site of recent high-mass star formation—is characterized by a significantly distorted field structure (see Figs. 2 and 6). This distortion appears to extend from the dense cloud core out to the boundary of the core region. It is significant that there is continuity between our optical polarimetry and the infrared polarimetry of Hodapp—which presumably probes deeper (in opacity) into the molecular cloud. This implies that both sets of polarization vectors are tracing the same gas structure, or, less likely, that the magnetic field remains unchanged between the low- and high-opacity regions. This same effect has also been observed in other dark clouds (cf. Goodman et al. 1992; Klebe & Jones 1990) but is not well understood.

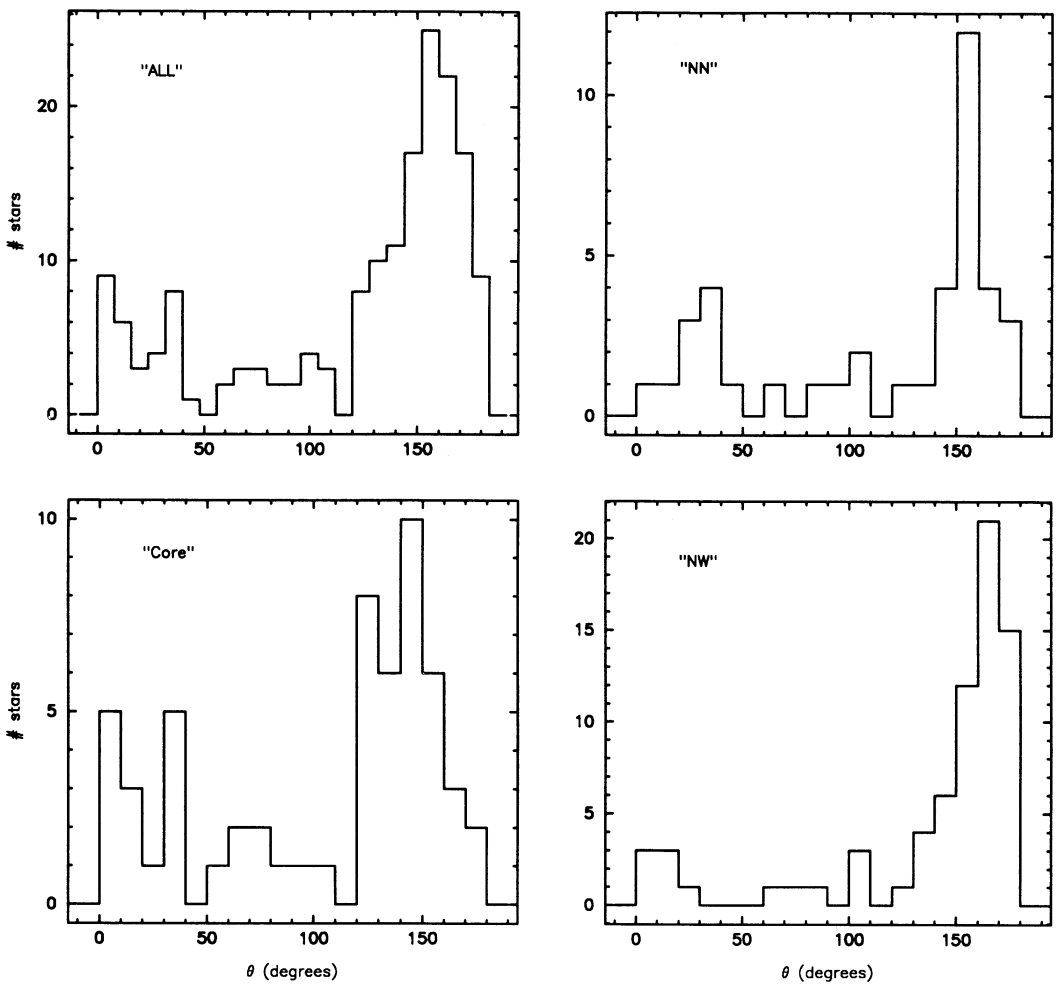

FIG. 7.—Distribution of angle of polarization, θ (degrees), for the Mon R2 sources (Table 1) given as histograms

As briefly discussed in the previous section, recent theoretical work shows that a distorted magnetic field is not an unexpected result in the event of cloud collapse. As noted in the review by Shu et al. (1987), in supercritical cloud collapse the magnetic forces are overwhelmed by the cloud gravitational forces resulting in a bending of the magnetic field, and subsequently, amplification of the field strength. The tension between the magnetic field lines tend to oppose the inward fall of gas so that the gravitational collapse is effectively "diluted." However, this configuration is eventually relaxed via ambipolar diffusion, and the magnetic forces are no longer dynamically important.

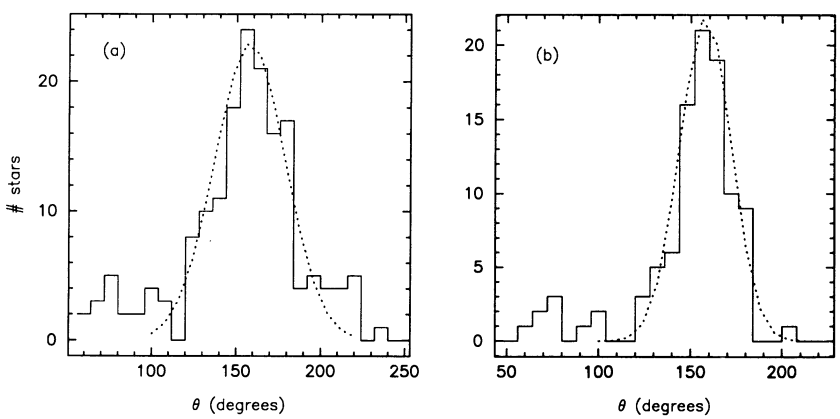

FIG. 8.—Distribution of angle of polarization for (*a*) all three fields combined and (*b*) the combined western halves of the three fields. A Gaussian fit (*dotted line*) to the distributions yields $\bar{\theta}_E = 159° \pm 1°, s = 0.37 \pm 0.01$ for the combined fields, and $\bar{\theta}_E = 158° \pm 1°, s = 0.24 \pm 0.01$ for the western-only half-fields.

There are a number of factors that potentially confuse the simple picture described above. These are all related to the fact that the physical environment of the Mon R2 cloud core is far from quiescent (as was once thought). In addition to turbulent gas motions, the dense core of Mon R2 possesses a massive bipolar molecular outflow, $\sim 10^{47}$ ergs (Bally & Lada 1983), by far the dominant energy source in the core. An outwardly radial-directed wind from the young object may transfer enough energy to the local surrounding media that it functions as the dominant form of cloud support (relative to gas turbulence or the magnetic field). It is interesting to note that the projected bipolar outflow axis and the projected magnetic field direction are along the same direction, which suggests a common physical origin. One possibility is that the outflowing gas from this object is preferentially expanding along the magnetic field—*which is also coincident with the direcion of the largest gas density gradient.* We have emphasized the latter point since the connection between the magnetic field and the outflow may only be indirect at best. As previously discussed in § 3.2, the inferred correlation between the observed polarization and the magnetic field geometry is complicated by the fact that the opacity in this region is large. As seen in the *R*-band images and in the molecular gas column density map, there are many dark clumps and filaments observed in projection across the Mon R2 field, and thus we are potentially measuring the integrated dichroic absorption of starlight through different magnetic field geometries along the line of sight of the molecular cloud. If the magnetic field decorrelation length is something like 1 or $2A_v$ (as suggested by Jones et al. 1992 as typical for molecular clouds) then the polarized light we measure should represent from as low as one to as high as four different field directions (in the random component of the field) and the dispersion in the angle of polarization from star to star should be correspondingly low to high. In the most extreme case, the polarization direction is dominated by the gas column density and less so by the underlying magnetic field structure. Instead of a distorted magnetic field morphology, the complex polarization in the northeast quadrant of the Core field may instead reflect the complex clumpy gas structure in this area. More likely, however, the angle of polarization we measure in this area represents some combination of a modified magnetic field structure and opacity effects, both associated with the embedded YSO cluster in the core of Mon R2 (and possibly related to a shock wave; see below). Empirically, we find that the total scatter seen in the distribution of angle of polarization for the "Core" field, $s = 0.40 \pm 0.02$ rad, is comparable to values measured in other active star formation regions (cf. VSS; Myers & Goodman 1991).

In the remaining areas of the Core field and in the western portions of the Mon R2 NW and NN fields, we find that the dispersion in the angle of polarization is much smaller, from 0.21 to 0.25 radians (e.g., Fig. 8*b*), which is comparable to that measured in less vigorous star-forming regions such as Taurus-Auriga (cf. Heyer et al. 1986; Myers & Goodman 1991). This result seems to suggest that the polarization vectors are tracing a uniform magnetic field structure, as least for the western portions of the three Mon R2 fields.

It is remarkable that the larger part of the magnetic field in Mon R2 appears to be azimuthal with the Galactic plane. This result is in accordance with the Parker instability (Parker 1966), where molecular clouds weigh down the magnetic field and constrain its structure along the plane of the Galaxy. Notably, this is not seen quite so clearly in Orion (VSS), another giant molecular cloud often connected with Mon R2 due to their unusually large dislocation from the Galactic plane. Some authors (cf. Franco et al. 1988) have proposed models explaining the common origin of the Mon R2 and Orion giant molecular clouds, while also directly or indirectly relating this "event" with that of Gould's belt. Notwithstanding the complexity of Orion's magnetic field structure, the coincidence of the magnetic field direction in Mon R2 and the Galactic plane direction is significant and needs to be investigated in other GMCs.

4.2. *Large-Scale Field Structure*

Recent observational results at millimeter wavelengths reveal that an expanding gas shell now dominates the Mon R2 GMC (Xie 1992; Xie & Goldsmith 1994). The expanding gas bubble is immense, $\sim 3°$ in diameter (crossing time of 5×10^6 yr), with a projected center (origin) $\sim 30'$ east of the cloud core and located behind the bulk of the Mon R2 cloud. The estimated mechanical energy of the shell is 10^{48}–10^{49} ergs. The western front of the bubble shell, corresponding to high-density gas $> 10^4$ cm^{-3} moving at 3.5–4.5 km s^{-1} (VLSR $\sim$ 11–14 km s^{-1}), is clearly seen as an opaque ridge in our Mon R2 NW and NN fields (Figs. 3 and 4). The authors argue that the main central core, including the outflow and embedded stellar cluster, forms a "peninsula" structure extending into the cavity or postshock region (see Fig. 6). The cavity side, oriented toward the east relative to our three polarimetric fields, is characterized as a hot low-density medium with H_2 densities less then 100 cm^{-3}. The eastern side of Mon R2 NN (Figs. 4 and 6) most dramatically illustrates the low extinction cavity region.

Since the magnetic field is coupled to the gas, the $\boldsymbol{B}$ field geometry should also be modified by the expanding gas shell. Shock waves can alter the velocity field and can deposit energy into the medium—either of these two mechanisms can result in a distorted field in the postshock region. The radio data provide compelling evidence that the large scale gas structure of Mon R2 has undergone asymmetric compression. It can be seen from Figure 6 that a curving ridge of dense gas extends northward from the core (southernmost box) through the center of the NW field and diagonally through the eastern side of the NN field. Figure 6 nicely illustrates the continuous, magnetic field structure slowly curving along the western side of the three CCD fields. Unfortunately, the gas kinematics are sufficiently complicated along the western shock front of Mon R2 (partly due to projection effects) that it is not altogether obvious which regions to the west of the opaque dust ridge (which we identify as the expanding shell) have been affected by the compression wave.

In principle the magnetic field distortion resulting from a shock wave depends on the angle between the ambient field direction and the shock front. The component of $\boldsymbol{B}$ parallel to the shock front is compressed and amplified, while the orthogonal component does not change. The supersonic expanding gas shell originates from a location east of three polarimetric fields. As already noted there appears to be significant distortion in the magnetic field within Mon R2 Core, in which the polarization vectors corresponding to the *northeast* quadrant are inclined $\sim 90°$ to the rest of the Core region (see Fig. 6). We have suggested that the bent field morphology is due (in part) to gravitational collapse, which may in turn be precipitated by a vector (asymmetric) force—the expanding gas shell. We caution, however, that it is not possible to separate the effects

(upon the magnetic field) of gravitational contraction from those of the shock wave.

In contrast to the well-defined $\boldsymbol{E}$ vector orientation for the western side of the three fields, the polarization results for the eastern side of the NW and NN field—corresponding to the evacuated side (in sky projection) of the expanding shell—is characterized by stars with relatively low percentage of polarization and, significantly, much higher dispersion in the angle of polarization. The low percentage of polarization in these regions is probably due to the relative paucity of gas and dust ($A_v < 3$)—most of which has been swept up by the expanding bubble shell. Under these circumstances, foreground interstellar clouds situated along the line of sight can have comparable polarizations to that of the molecular cloud itself. The net result would be an increase in angle of polarization dispersion. In addition to foreground cloud contamination, hot and turbulent gas in the postshock region may also contribute to a large dispersion in $\bar{\theta}$. It is interesting to note that many of the polarization vectors are aligned parallel to the dense ridge bisecting the fields, which suggests that the magnetic field has undergone a counterclockwise distortion of $\sim 40°$–$60°$. We do not believe, however, that much significance should be attached to this result since the sample is small and the dispersion in the distribution of θ is large.

We also draw attention to a feature seen in the NW field. The average angle polarization for the sources located in the southwest quadrant of Mon R2 NW is $165° \pm 10°$ (see Fig. 7), which is offset $\sim 15°$ counterclockwise from the average $\boldsymbol{B}_\perp$ field direction computed for all three fields (west of the gas ridge; see Figs. 6 and 8). We speculate that the magnetic field in this quadrant has been altered by the expanding gas shell. The ^{12}CO observations (Fig. 6) and particularly, the ^{13}CO gas column densities (Xie 1992) indicate that this region *is* part of the expanding gas shell. The polarization vectors just to the south of this quadrant (and slightly east, corresponding to the northwest quadrant of Mon R2 Core) are aligned more to the west. Are we viewing the projected curvature in the shock compressed shell? Additional polarimetric measurements of fields located to the south and west of the expanding shell are necessary in order to establish field curvature. Further observations are also necessary to firmly establish the $\boldsymbol{B}_\perp$ geometry corresponding to ambient primordial field of Mon R2.

In the context of an energetic shock wave propagating through the Mon R2 giant molecular cloud, the magnetic field lines have been distorted by the expanding shell resulting in a compressed magnetic field structure near the interface. A possible outcome of just such a distortion is local clumping of the gas and subsequent gravitational collapse along the direction of the field. This may have recently occurred in the Mon R2 complex. Aligned along the *eastern* edge of the gas ridge that extends into the NW and NN fields (see Fig. 6), in the postshock region, there are tens of *IRAS* point sources which are presumed to be deeply embedded young stars (Xie 1992). In contrast, there are few *IRAS* point sources anywhere along the western side of the GMC. The location and age of these sources suggest shock-triggered star formation, and to which we suggest that the primary form of cloud support, the magnetic field, has been significantly altered by the shock. This mode of star formation is certain to be common throughout the Galaxy. In a polarization study of the CMa R1 association, for example, Vrba, Baierlein, & Herbst (1987) similarly find that the underlying magnetic field has been distorted by a shock wave. In the case of CMA R1, a proximal supernova provides the vectored force that distorts the field and which (presumably) triggers a burst of star formation interior to the "amplified" magnetic field. Both in Mon R2 and CMa R1, a large-scale structure has significantly altered the cloud environment, from the largest size scales, in which we observe filamentary gas morphology and curvature in the ambient magnetic field geometry, to the smallest, in which we detect local clumping of gas and recent star formation.

Given the energetics of Mon R2 and complications due to the massive bipolar outflow and expanding bubble shell, it remains a very difficult task to understand the magnetic field geometry. Nevertheless, the results of this study, in concert with those of the central Orion A molecular cloud (Novak et al. 1989), suggest that magnetic fields are a dynamically important component to massive star formation regions.

5. SUMMARY

We have carried out polarimetric observations to study the magnetic field structure of the Mon R2 giant molecular cloud. The polarimetry was calibrated using a new technique that relies on obtaining photometry of stars simultaneously with polarimetric photometry of object fields, thus providing an accurate means to measure the polarization of electric vectors for stars observed through the Mon R2 cloud. The main points and conclusions of this work may be summarized as follows:

1. We obtained deep R-band CCD polarimetry of three fields located toward the Mon R2 molecular cloud, covering a total area of 0.5 deg^2. The polarimetry was complete for all stars brighter than $R \sim 18$, comprising more than 600 stars. Of this total, ~ 180 stars had measured polarizations with $\geq 3\,\sigma$ accuracy and $P > 1\%$.

2. The polarizations for sources observed through the Mon R2 molecular cloud have values consistent with selective extinction via a grain alignment mechanism similar to that functioning in the general interstellar medium. The overall trend is of increasing polarization with extinction, although the scatter is very large. One possibility is that for the dense regions, the efficiency of polarization is diminished in comparison to that of more diffuse areas. It is also possible that the magnetic field geometry decorellates in the higher opacity regions, effectively rendering our optical polarimetry less sensitive to the magnetic field in these dense structures.

3. The Mon R2 "core" magnetic field geometry is comprised of three distinct features as inferred from the polarization vectors: general alignment parallel to the long axis of the filament, coincidence with the bipolar molecular outflow axis and the local Galactic magnetic field, and finally, distortion or bending toward the long axis of the cloud core. The latter two features suggest that magnetic fields play an important role in massive star formation regions. In addition to gravitational and rotational stresses, another mechanism that likely contributes to the distorted magnetic field is an energetic shock wave, which recent millimeter-wave observations reveal is now dominating the Mon R2 complex.

4. The polarimetry suggests continuity in core general magnetic field structure. The mean angle of polarization for the three fields is $158° \pm 33°$, which is roughly coincident with the local Galactic magnetic field at 155°. The dispersion in the distribution of angle of polarization is similar to that found in the Orion GMC. The mean angle of polarization for stars located along the western side of the three CCD fields is $\sim 157°$ with a standard deviation of 22°. To the north of the Mon R2

core region, the polarization vectors exhibit a substantial increase in scatter, as seen from west to east across the CCD fields. These CCD fields are bisected by a dense ridge of gas which appears to be the boundary of a shock-compressed shell. Our polarimetry suggests that the expanding shell has distorted the magnetic field lines extending from the core to the northern gas structure comprising Mon R2. One possible consequence of the shock-altered magnetic field is a recent burst of star formation along the eastern boundary of the gas ridge.

We would like to thank Dave Silva and George Jacoby for their on-site technical support at Kitt Peak National Observatory. T. H. J. would like to thank Mark Heyer, Mike Meyer, and Steve Strom for their helpful comments. We would also like to thank the referee for providing several important comments. This work was carried out in part at the Jet Propulsion Laboratory, California Institute of Technology, under a contract with the National Aeronautics and Space Administration.

REFERENCES

Aitken, D. K., Wright, C. M., Smith, C. H., & Roche, P. F. 1993, MNRAS, 262, 456
Aspin, C., & Walther, D. M. 1990, A&A, 235, 387
Bally, J., & Lada, C. J. 1983, ApJ, 265, 824
Bally, J., Langer, W. D., & Liu, W. 1991, ApJ, 383, 645
Beckwith, S., Evans, N. J., Becklin, E. E., & Neugebauer, G. 1976, ApJ, 209, 390
Clayton, G. C., & Cardelli, J. A. 1988, AJ, 96, 695
Davis, L., & Greenstein, J. L. 1951, ApJ, 114, 206
Dickman, R. L. 1978, AJ, 83, 363
Dyck, H. M., Forbes, F. F., & Shawl, S. J. 1971, AJ, 76, 901
Dyck, H. M., & Lonsdale, C. J. 1979, AJ, 84, 1339
Eggen, O. J., & Sandage, A. R. 1964, ApJ, 140, 130
Franco, J., Tenorio-Tagle, G., Bodenheimer, P., Rozyczka, M., & Mirabel, I. F. 1988, ApJ, 333, 826
Gillis, J., Mestel, L., & Paris, R. B. 1974, A&AS, 27, 167
Goodman, A. A., Bastien, P., Myers, P. C., & Menard, F. 1990, ApJ, 359, 363
Goodman, A. A., Jones, T. J., Lada, E. A., & Myers, P. C. 1992, ApJ, 399, 108
Hackwell, J. A., Grasdalen, G. L., & Gehrz, R. 1982, ApJ, 252, 250
Heiles, C., Goodman, A. A., McKee, C., & Zweibel, E. G. 1992, in Protostars and Planets III, ed. M. C. Matthews & E. H. Levy (Tucson: Univ. of Arizona Press), 279
Herbst, W., & Racine, R. 1976, AJ, 81, 840
Heyer, M. H., Snell, R. L., Goldsmith, P. F., Strom, S. E., & Strom, K. M. 1986, ApJ, 308, 134
Hildebrand, R. H. 1988, QJRAS, 29, 327
Hiltner, W. A. 1956, ApJS, 2, 389
Hodapp, K. W. 1984, A&A, 141, 225
———. 1987, A&A, 172, 304
Janes, K. A., & Smith, G. H. 1984, AJ, 89, 487
Jarrett, T. H. 1992, Ph.D. thesis, Univ. of Massachusetts
Jones, T. J. 1989, ApJ, 346, 728
Jones, T. J., Klebe, D., & Dickey, J. M. 1992, ApJ, 389, 602
Klebe, D., & Jones, T. J. 1990, AJ, 99, 638
Kutner, M. L., & Tucker, K. D. 1975, ApJ, 199, 79
Landolt, A. U. 1983, AJ, 88, 439
Lee, H. M., & Draine, B. T. 1985, ApJ, 290, 211
Loren, R. B. 1977, ApJ, 215, 129
Maddalena, R. J., Morris, M., Moscowitz, J., & Thaddeus, P. 1986, ApJ, 303, 375
Mathewson, D. S., & Ford, V. L. 1970, MNRAS, 74, 139
Mouschovias, T. C. 1976, ApJ, 206, 753
———. 1978, in Protostars and Planets, ed. T. Gehrels (Tucson: Univ. of Arizona Press), 209
Myers, P. C., & Goodman, A. A. 1988, ApJ, 326, L27
———. 1991, ApJ, 373, 509
Myers-Rice, B. A., & Lada, C. J. 1991, ApJ, 368, 445
Novak, G., Gonatas, D. P., Hildebrand, R. H., Platt, S. R., & Dragovan, M. 1989, ApJ, 345, 802
Novak, G., Predmore, C. R., & Goldsmith, P. F. 1990, ApJ, 355, 166
Novak, G., & Jarrett, T. H. 1994, J. Appl. Opt., submitted
Parker, E. E. 1966, ApJ, 145, 811
Sato, S., Tamura, M., Nagata, T., Kaifu, N., Hough, J., McLean, I. S., Garden, R. P., & Gatley, I. 1988, MNRAS, 230, 321
Schoening, B., et al. 1990, Operation of the CCD Direct Imaging Camera for the 0.9 Meter Telescope Kitt Peak National Observatory
Serkowski, K. 1974, Polarization Techniques, in Methods of Experimental Physics, 12A, ed. N. Carleton (New York: Academic), 348
Serkowski, K., Mathewson, D. S., & Ford, V. L. 1975, ApJ, 196, 261
Shu, F. H., Adams, F. C., & Lizano, S. 1987, ARA&A, 25, 23
Shu, F. H., Lizano, S., Adams, F. C., & Ruden, S. P. 1988, in Formation and Evolution of Low Mass Stars, ed. A. K. Dupree & M. T. V. T. Lago (Dordrecht: Kluwer), 123
Strom, K. M., Strom, S. E., Wolff, S., Morgan, J., & Wenz, M. 1986, ApJS, 62, 39
Thronson, H. A., Gatley, I., Harvey, P. M., Sellgren, K., & Werner, M. W. 1980, ApJ, 237, 66
Vrba, F. J., Baierlein, R., & Herbst, W. 1987, ApJ, 317, 207
Vrba, F. J., Strom, S. E., & Strom, K. M. 1976, AJ, 81, 958
———. 1988, AJ, 96, 680 (VSS)
Xie, T. 1992, Ph.D. thesis, Univ. of Massachusetts
Xie, T., & Goldsmith, P. F. 1994, ApJ, in press
Xie, T., Goldsmith, P. F., & Patel, N. 1993, ApJ, 419, L33
Zaritsky, D., Shaya, E. J., Scoville, N. Z., Sargent, A. I., & Tytler, D. 1987, AJ, 93, 1514